Science Advances
AAAS

advances.sciencemag.org/cgi/content/full/6/17/eaaz5413/DC1

Supplementary Materials for

Colored and paintable bilayer coatings with high solar-infrared reflectance for efficient cooling

Yijun Chen, Jyotirmoy Mandal, Wenxi Li, Ajani Smith-Washington, Cheng-Chia Tsai, Wenlong Huang, Sajan Shrestha, Nanfang Yu*, Ray P. S. Han, Anyuan Cao, Yuan Yang*

*Corresponding author. Email: yy2664@columbia.edu (Y.Y.); ny2214@columbia.edu (N.Y.)

Published 24 April 2020, *Sci. Adv.* **6**, eaaz5413 (2020)
DOI: 10.1126/sciadv.aaz5413

This PDF file includes:

Figs. S1 to S19
Tables S1 to S3
Notes S1 to S6
References

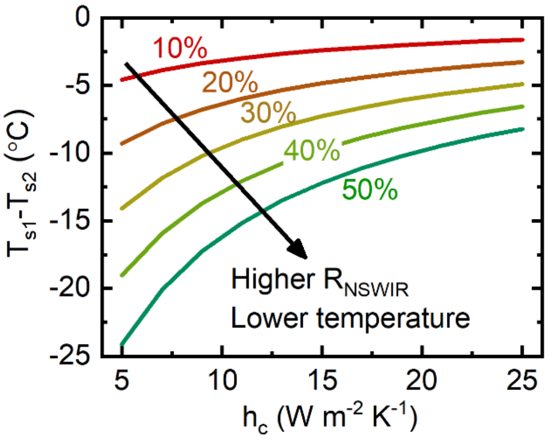

Fig. S1. The calculated temperature difference between two surfaces with 10%, 20%, 30%, 40% and 50% difference in R_{NSWIR} at different h_c (convective heat transfer coefficient). T_{s1} and T_{s2} correspond to the temperature of the cool and hot surface respectively. The calculation process is described in **Supplementary Note 1.** Assuming the two surfaces' solar reflectance spectrum only has difference in the NSWIR part, and they have the same thermal emittance of 0.9. The solar irradiance is set as 1000 W m^{-2} and the temperature of the hot sample is 40 °C. The calculation results show that a lower temperature could be achieved with increasing reflectance in the NSWIR wavelengths, and the temperatures of the two surfaces vary more at a less convective condition.

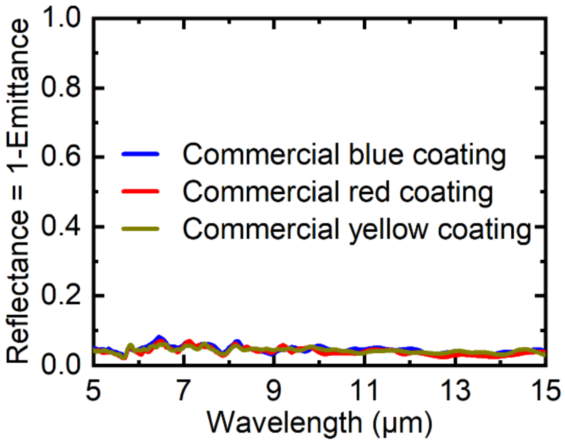

Fig. S2. Infrared reflectance spectrum of the commercial colored paint coatings, showing their high broadband thermal emittance.

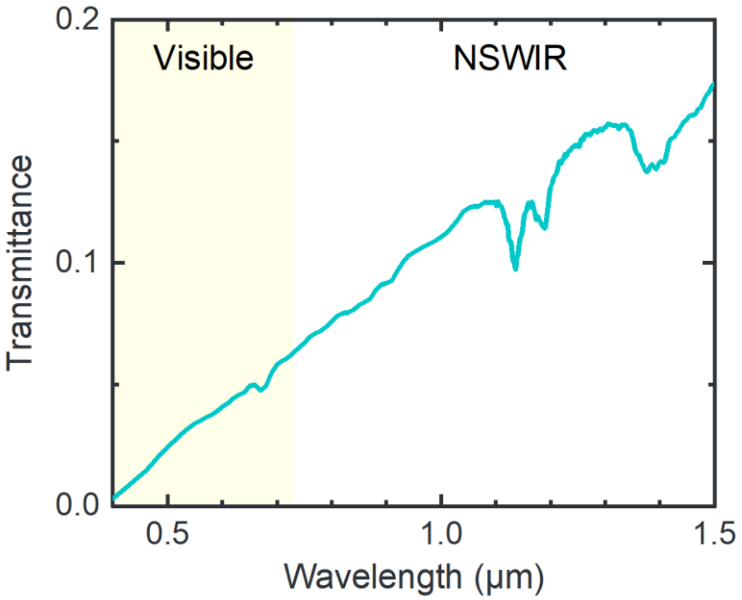

Fig. S3. Transmittance spectrum of the TiO_2 paint film, showing the deeper penetration by longer NSWIR wavelengths compared to visible light. Similar phenomena are observed for porous polymer films as well (*11*).

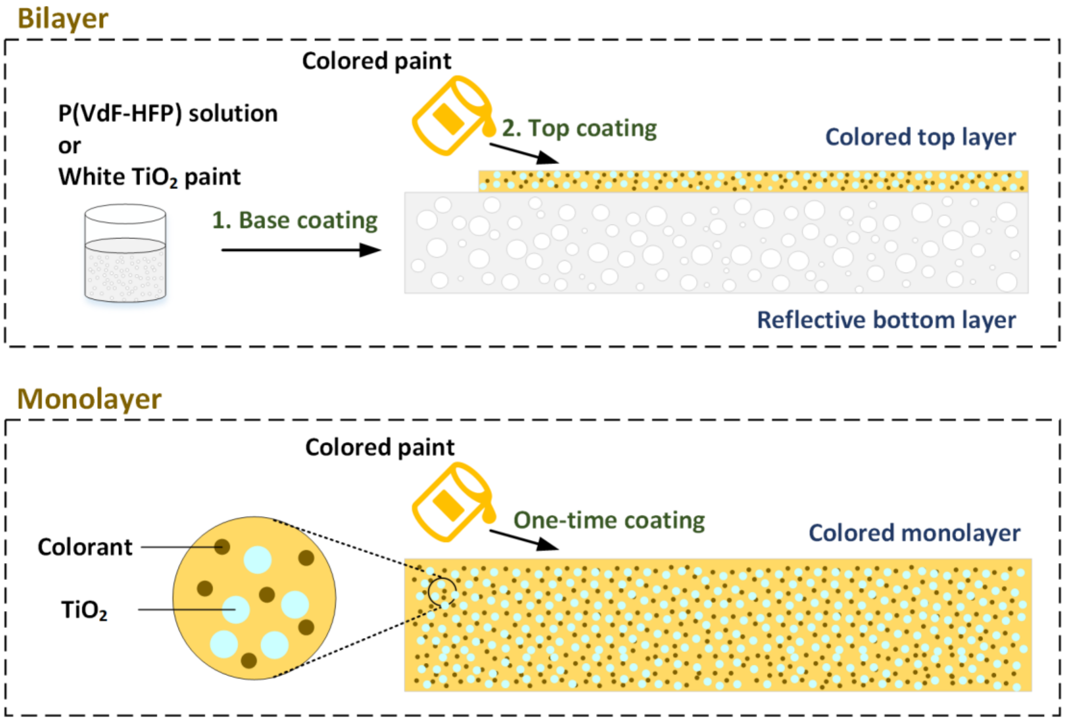

Fig. S4. Schematic of the fabrication process of the colored cooling coatings. Top: the fabrication process of the bilayer coating. Bottom: the fabrication process of the monolayer coating.

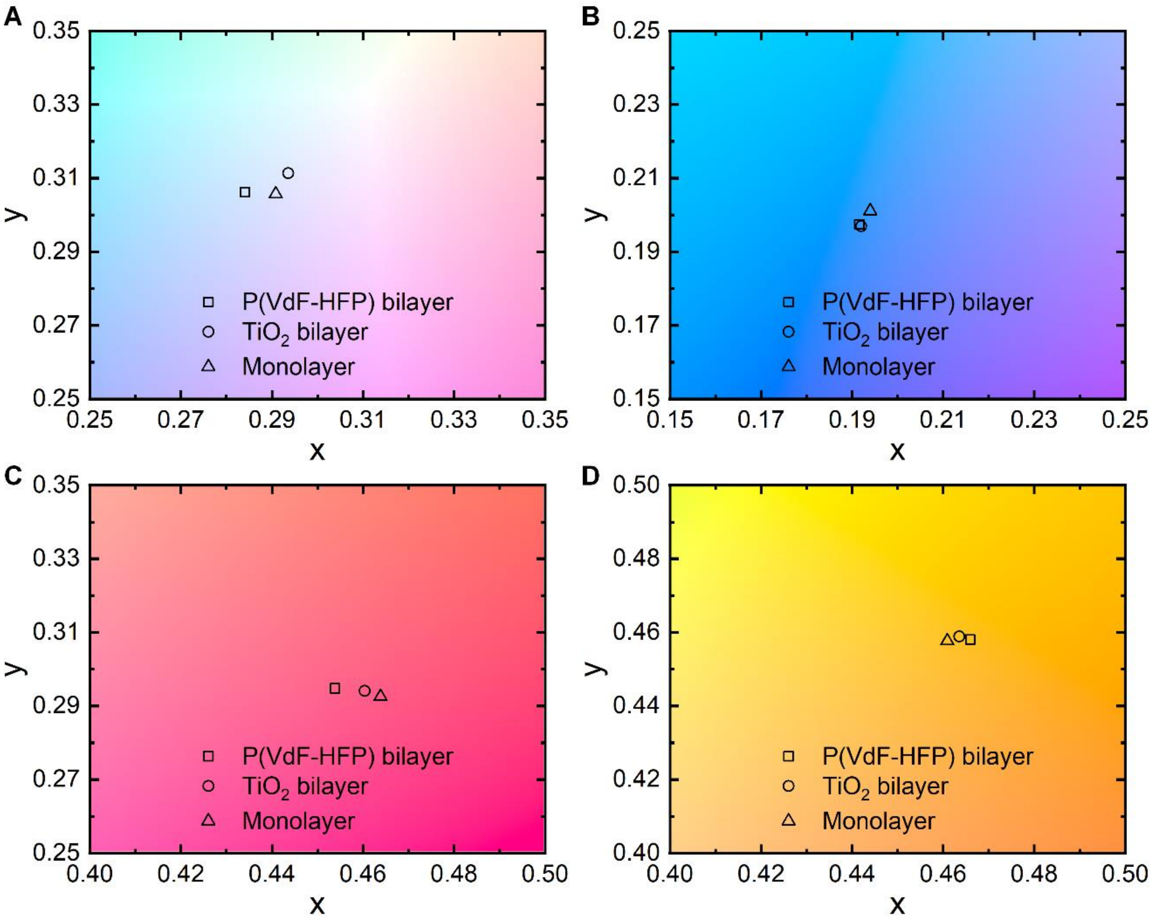

Fig. S5. Zoomed-in CIE 1931 color space figures of the colored coatings. (**A** to **D**) The chromaticity values of the black (**A**), blue (**B**), red (**C**) and yellow (**D**) coatings, indicating a near-identical color in each group of samples.

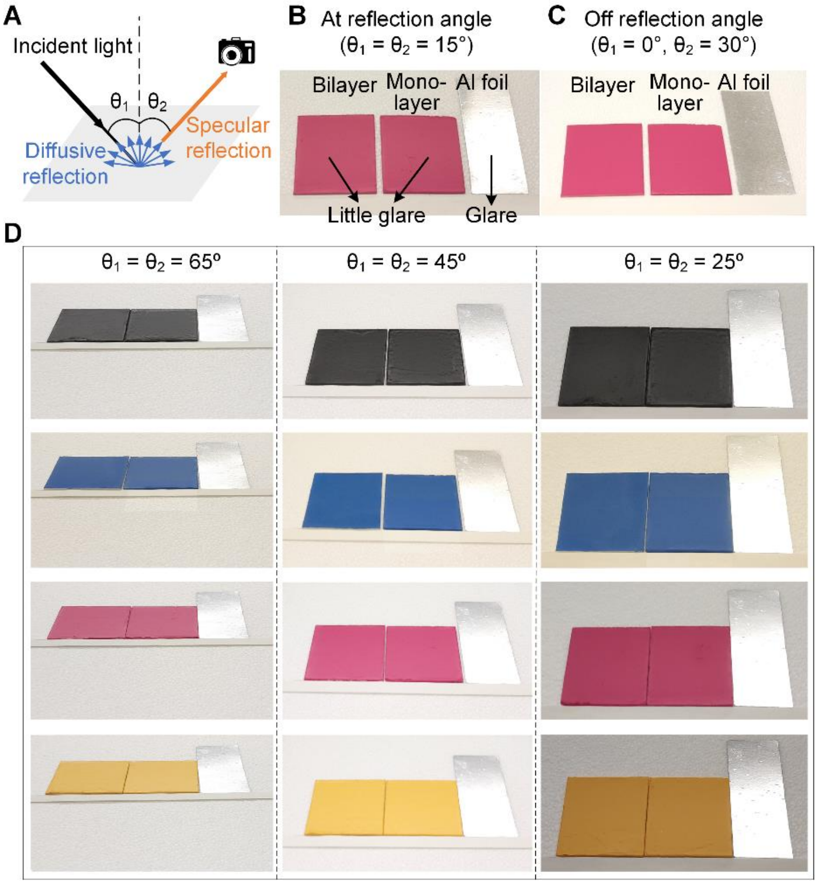

Fig. S6. Photographs of the monolayer and P(VdF-HFP)-based bilayer samples at different angles to demonstrate the lack of glare off the colored coatings. (**A**) Schematic of the setup. (**B** and **C**) Photographs of the coatings in (B) and off (C) the reflection direction. (**D**) Photographs of the coatings of all four colors along the direction of specular reflection for incidence angles of 25°, 45° and 65°. Photo credits: (B to D) Yijun Chen, Columbia University.

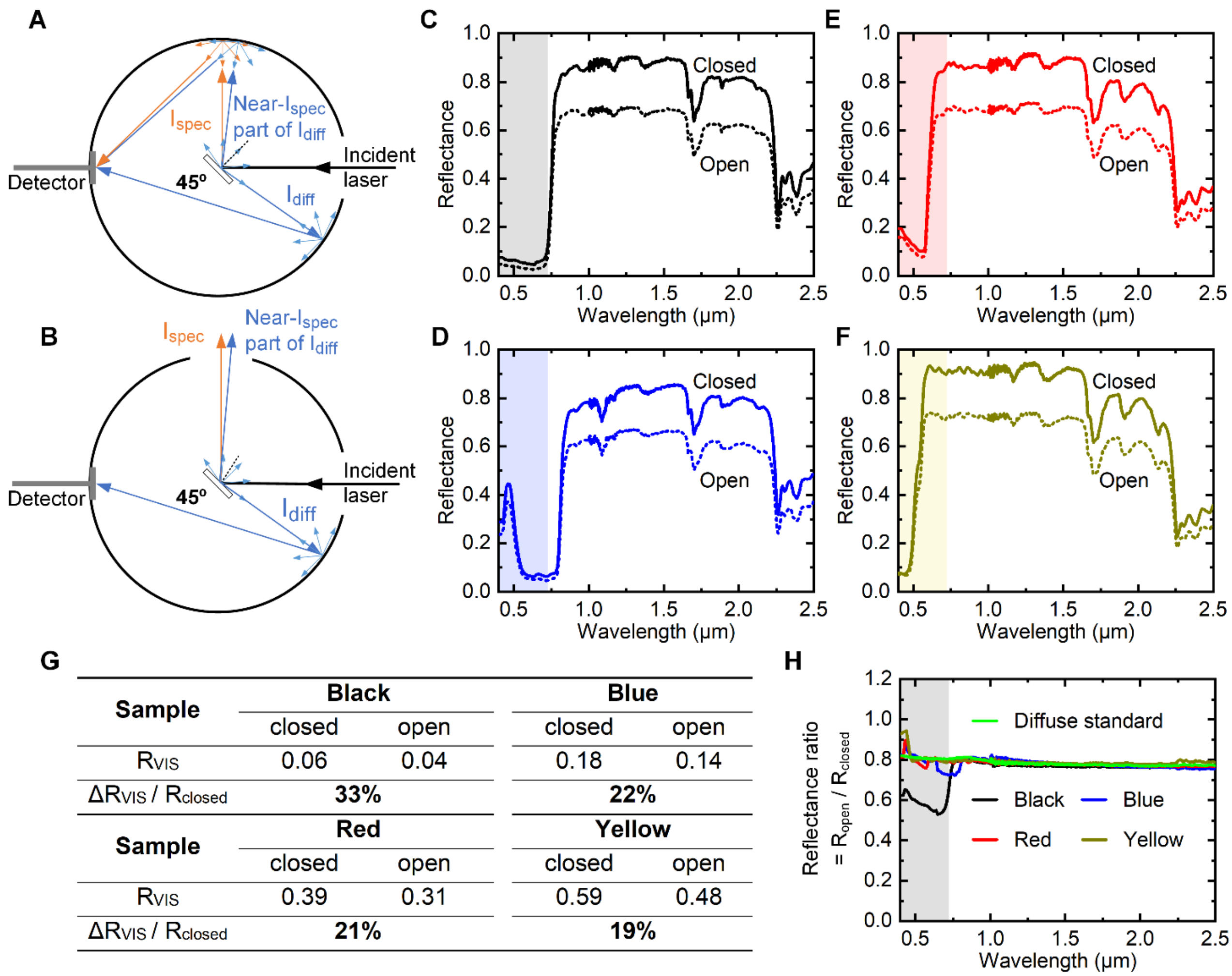

Sample	Black		Blue	
	closed	open	closed	open
R_{VIS}	0.06	0.04	0.18	0.14
ΔR_{VIS} / R_{closed}	**33%**		**22%**	
Sample	**Red**		**Yellow**	
	closed	open	closed	open
R_{VIS}	0.39	0.31	0.59	0.48
ΔR_{VIS} / R_{closed}	**21%**		**19%**	

Fig. S7. Investigation of the specularity of the P(VdF-HFP)-based bilayer coatings at 45° tilt. (**A** and **B**) Comparison of the light path in the integrating sphere with the top port open (A) and closed (B) when the sample is placed at 45° tilt. (**C** to **F**) Reflectance spectra of the black (C), blue (D), red (E) and yellow (F) coatings in the two cases. (**G**) Calculated R_{VIS} of the coatings based on the spectra (C to F) with the top port closed and open, showing the difference between the two cases is close to that of the diffuse reflectance standard (**H**). ΔR_{VIS} / R_{closed} = (R_{closed} - R_{open}) / R_{closed}, and Reflectance ratio = R_{open} / R_{closed}.

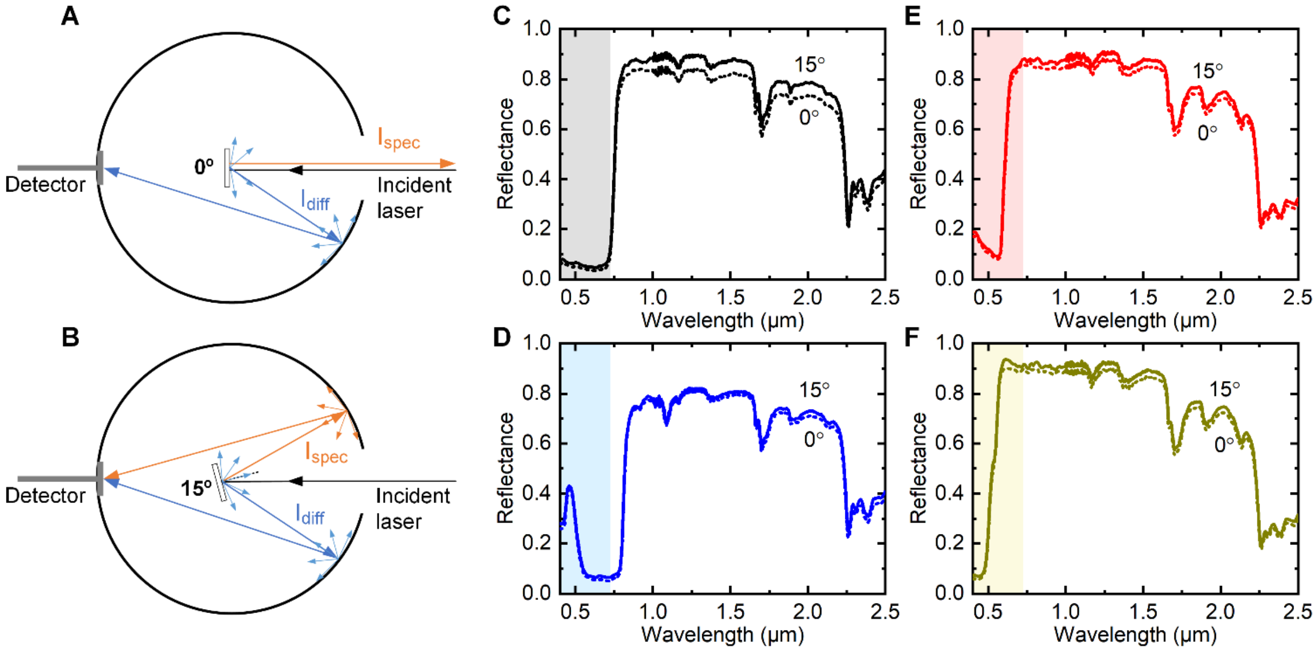

Fig. S8. Investigation of the specularity of the P(VdF-HFP)-based bilayer coatings at normal incidence. (**A** and **B**) Comparison of the light path in the integrating sphere with the sample tilting at an angle of 0º (A) and 15º (B). (**C** to **F**) Reflectance spectra of the black (C), blue (D), red (E) and yellow (F) coatings in the two cases. The difference between the 15˚ and 0˚ measurements is very small, indicating that the specular component at normal incidence is small as well.

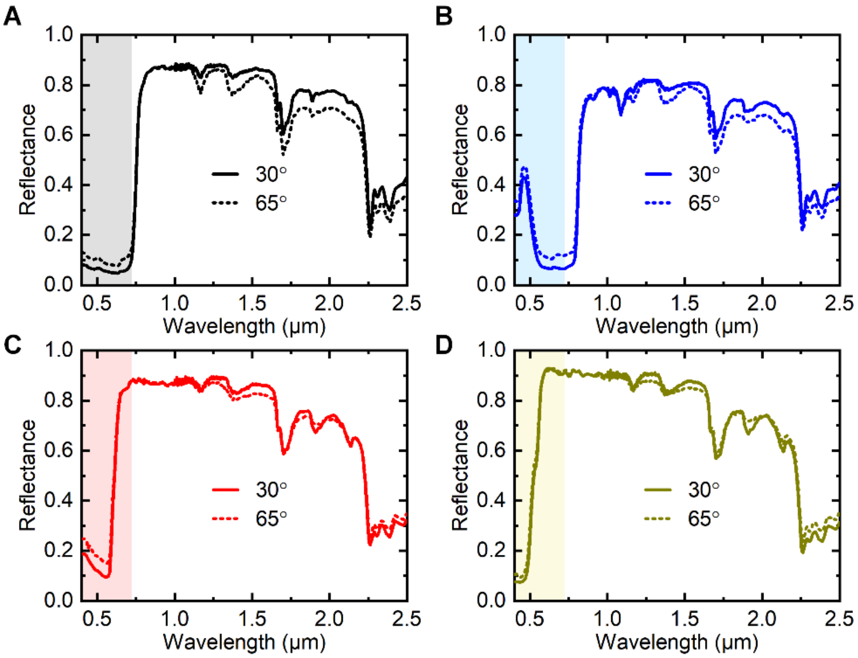

Fig. S9. The reflectance spectrum of the P(VdF-HFP)-based bilayer coatings at 65º and 30° tilt. (**A** to **D**) The spectrum of the black (A), blue (B), red (C) and yellow (D) coatings, showing that glare does not significantly increase at higher angles.

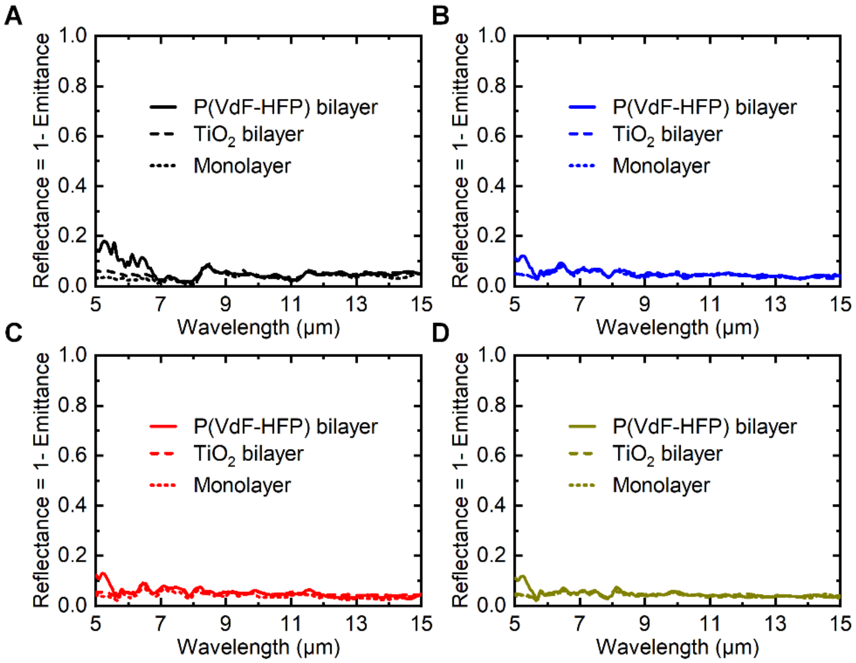

Fig. S10. Infrared reflectance spectrum of the different coatings. (**A** to **D**) The spectrum of bilayer and monolayer coatings of black (A), blue (B), red (C) and yellow (D) colors, showing their high broadband thermal emittances. As the temperatures of our colored coatings under sunlight are normally above the ambient, such high broadband emittance is more desirable for cooling than selective LWIR emittance (*6*).

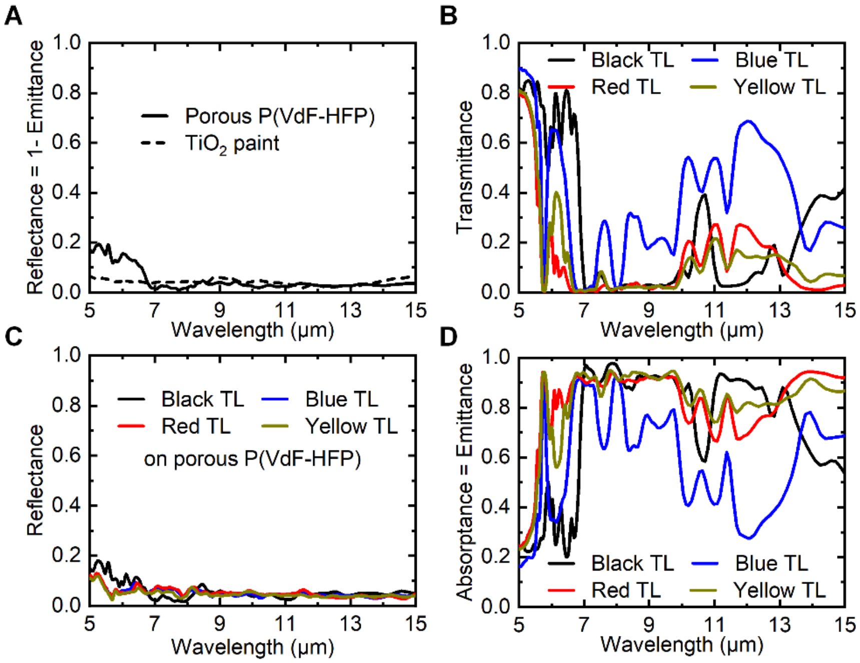

Fig. S11. Charaterization of the infrared emittance of the colored top-layers (TL). (**A**) Infrared reflectance spectra of the porous P(VdF-HFP) and TiO_2 paint underlayers. (**B**) Infrared transmittance spectra of the colored top-layers. (**C**) Infrared reflectance spectra of the top-layer, measured by putting the layers on IR-absorptive porous P(VdF-HFP). (**D**) Calculated infrared absorptance spectra of the colored top-layers based on the results in (B) and (C).

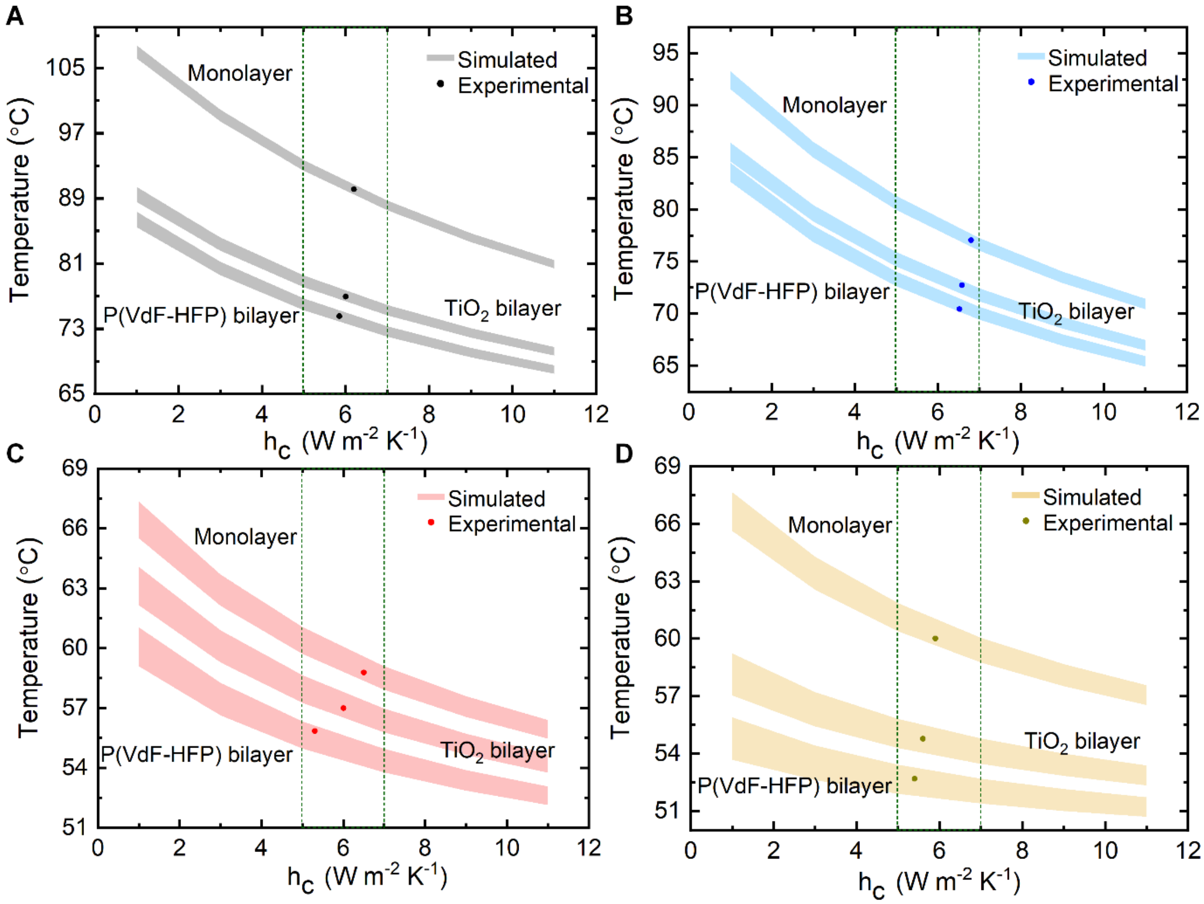

Fig. S12. Experimental and computed temperatures of the bilayer and monolayer colored coatings. (**A** to **D**) The results of the black (A), blue (B), red (C) and yellow (D) coatings at different convection conditions. The strips are computed temperature for a certain h_c derived from the COMSOL simulation. The width of the strip is based on an uncertainty of 0.01 in the samples' solar reflectance. For all samples, the experimental values locate in the strips within a h_c range of 5-7 W m^{-2} K^{-1}, indicating a good agreement between theoretical simulation and experimental data.

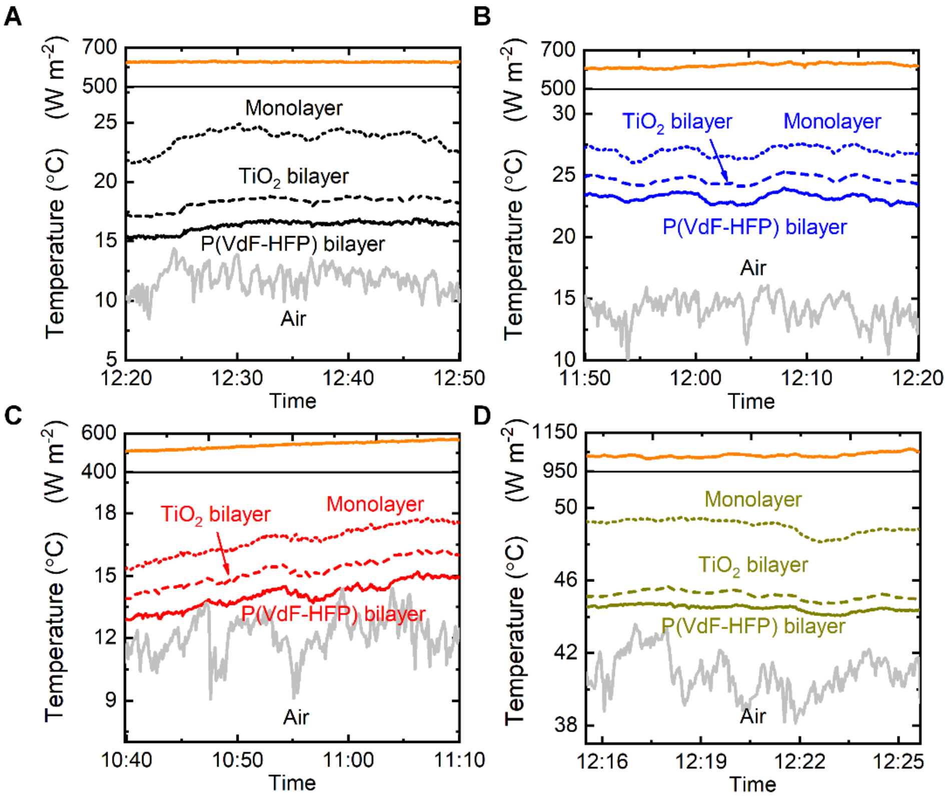

Fig. S13. Field tests of the different coatings without PE cover. (**A** to **D**) The black (**A**), blue (**B**), red (**C**) and yellow (**D**) coatings, tested in New York City on November 1st, November 2nd, November 2nd, and June 27th, 2019, respectively.

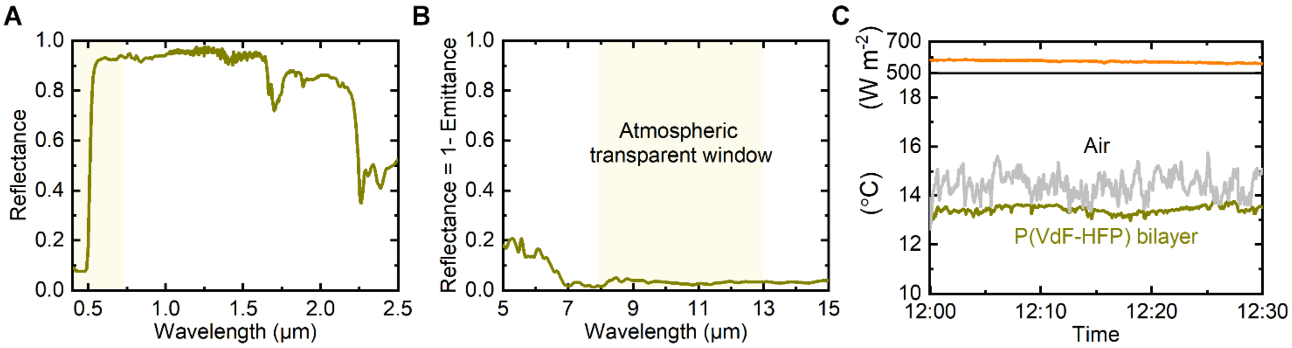

Fig. S14. Optical measurements and field test of a light yellow bilayer coating. The coating is fabricated by dispersing Dalamar Yellow colorants in transparent P(VdF-HFP) matrix to make a light yellow top-layer atop porous P(VdF-HFP). The resulting bilayer shows a R_{solar} of 0.80 (**A**) and broadband thermal emittance (5-15 μm) of 0.96 (**B**) and achieves an average temperature lowering of 1.0 ℃ below the ambient air under ~574 W m^{-2} solar irradiation without PE cover (**C**). The field test was conducted in New York City on November 4th.

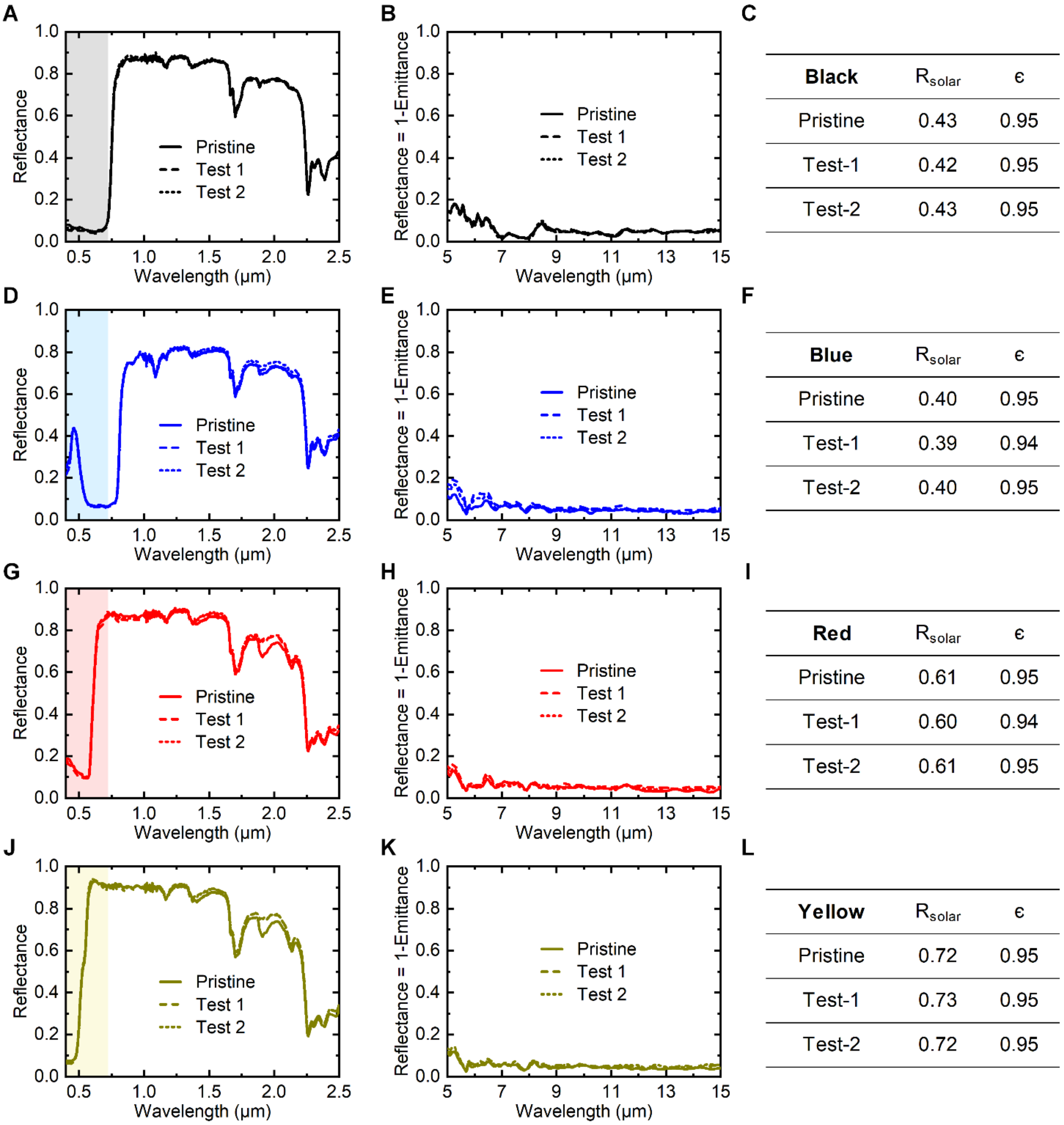

Black	R_{solar}	ϵ
Pristine	0.43	0.95
Test-1	0.42	0.95
Test-2	0.43	0.95

Blue	R_{solar}	ϵ
Pristine	0.40	0.95
Test-1	0.39	0.94
Test-2	0.40	0.95

Red	R_{solar}	ϵ
Pristine	0.61	0.95
Test-1	0.60	0.94
Test-2	0.61	0.95

Yellow	R_{solar}	ϵ
Pristine	0.72	0.95
Test-1	0.73	0.95
Test-2	0.72	0.95

Fig. S15. Optical measurements of the P(VdF-HFP)-based bilayer coatings before and after stability tests. (**A** to **L**) Measured solar reflectance and thermal emittance spectrum, and summarized R_{solar} and ϵ values of the black (**A** to **C**), blue (**D** to **F**), red (**G** to **I**) and yellow (**J** to **L**) coatings. Test 1 involved putting samples outdoors and exposed to the sky, while Test 2 involved putting samples in an oven at a constant temperature of 60 °C. Both tests lasted for 30 days. The top-coats for the samples were made using commerical paints, which are designed for stability, and the nearly unchanged performance after the tests indicate that the durability of the top-layer extends to the bilayer as a whole. The use of weather-resistant P(VdF-HFP) (*41*, *42*) could also contribute to the stablity.

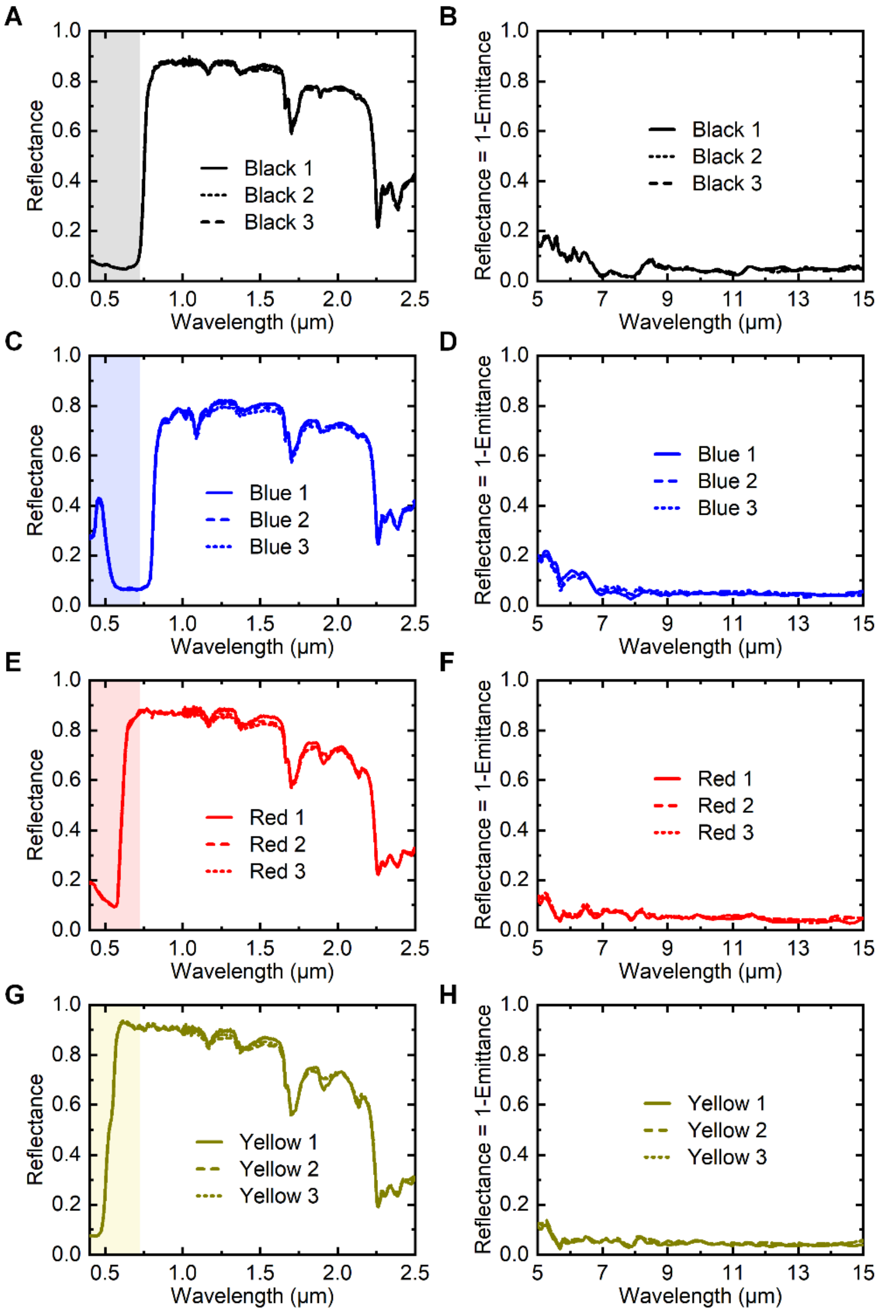

Fig. S16. Optical measurements of three different samples fabricated with the same coating procedure. (**A** to **H**) The solar reflectance and thermal emittance of the black (A and B), blue (C and D), red (E and F), and yellow (G and H) porous P(VdF-HFP)-based bilayer coatings. As shown, for each color, three samples exhibit near-identical optical properties in the solar wavelengths and infrared thermal wavelengths, indicating repeatability of the process.

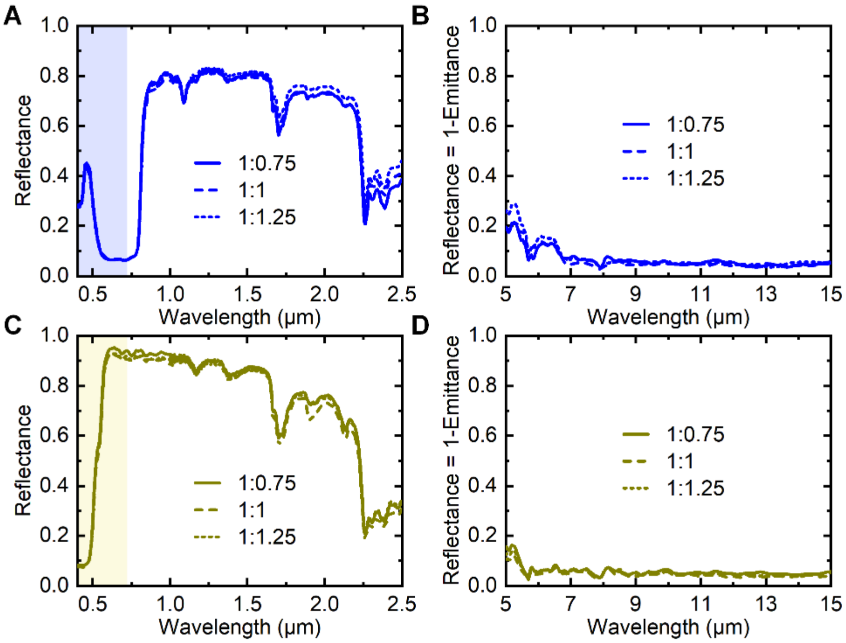

Fig. S17. Optical measurements of the P(VdF-HFP)-based bilayers fabricated with different P(VdF-HFP) : water ratios. (**A** to **D**) The solar reflectance and thermal emittance of the blue (A and B) and yellow (C and D) coatings, showing that the effect of changing composition of the precursor is minimal.

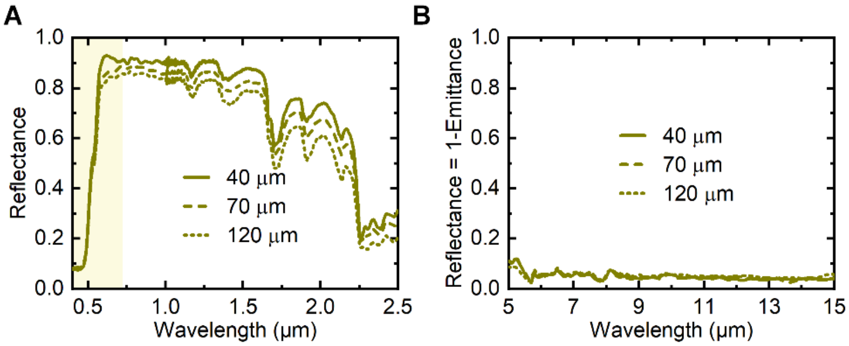

Fig. S18. Optical measurements of the P(VdF-HFP)-based yellow bilayers comprising top-layers with different thicknesses. (**A** and **B**) The solar reflectance (A) and thermal emittance (B) of the bilayers. As evident, changing the thickness of the top layer by ~3 times only reduces the NSWIR reflectance by ~10% and no distinct emittance changes are observed, showing the technique is quite insensitive to top-layer thickness in terms of R_{NSWIR} and thermal emittance.

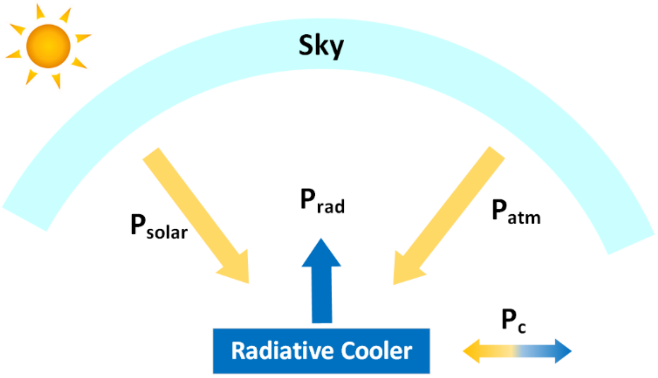

Fig. S19. Schematic of the heat transfer process in a radiative cooler under sunlight.

Table S1. Normalized chromaticity values (x, y) and lightness values (L) of the colored coatings. P, T and M correspond to the porous P(VdF-HFP)-based bilayer, TiO_2-based bilayer and monolayer.

Sample	**Black**			**Blue**			**Red**			**Yellow**		
	P	T	M	P	T	M	P	T	M	P	T	M
x	0.28	0.29	0.29	0.19	0.19	0.19	0.45	0.46	0.46	0.47	0.46	0.46
y	0.31	0.31	0.31	0.20	0.20	0.20	0.29	0.29	0.29	0.46	0.46	0.46
L	28.5	27.5	25.3	43.0	42.3	40.3	51.3	50.3	48.4	85.0	84.3	81.8

Table S2. The thermal emittance (5-15 μm) of the porous P(VdF-HFP) or TiO_2 paint coating underlayer (ϵ_{under}), the colored top-layer (ϵ_{top}), and their combination (ϵ_{bi}). P, T and M correspond to the porous P(VdF-HFP)-based bilayer, TiO_2-based bilayer and monolayer. For M, there is only one layer.

Sample	**Black**			**Blue**			**Red**			**Yellow**		
	P	T	M	P	T	M	P	T	M	P	T	M
ϵ_{under}	0.96	0.96	0.96	0.96	0.96	0.95	0.96	0.96	0.96	0.96	0.96	0.96
ϵ_{top}	0.78			0.59			0.84			0.85		
ϵ_{bi}	0.95	0.95		0.95	0.95		0.95	0.95		0.95	0.96	

Table S3. The broadband thermal emittance ($\epsilon_{broadband}$, 5-15 µm), and selective LWIR emittance (ϵ_{LWIR}, 8-13 µm) of the colored coatings. P, T and M correspond to the porous P(VdF-HFP)-based bilayer, TiO_2-based bilayer and monolayer, respectively.

Sample	**Black**			**Blue**			**Red**			**Yellow**		
	P	T	M	P	T	M	P	T	M	P	T	M
$\epsilon_{broadband}$	0.95	0.95	0.96	0.95	0.95	0.95	0.95	0.95	0.96	0.96	0.96	0.96
ϵ_{LWIR}	0.95	0.95	0.96	0.95	0.95	0.95	0.95	0.95	0.96	0.95	0.96	0.96

Supplementary Note 1: Theoretical Calculation of Temperature Difference between Two Surfaces

According to the energy conservation law, the net radiative cooling power of the radiator should be zero at the thermal equilibrium, indicating the following 4 energy flows reach a balance (**Fig. S19**):

$$P_{solar} + P_{atm}(T_a) = P_{rad}(T_s) + P_c$$

where P_{solar} and P_{atm} are the absorbed solar energy and atmospheric radiation respectively, P_{rad} is the heat that sample radiates to the outer space, P_c is the non-radiative heat transfer loss to ambient, T_a and T_s are the temperature of the ambient and the sample respectively.

Specifically,

$$P_{solar} = P_{ir}(1 - \bar{R}\ )$$

where P_{ir} is the total solar radiation and $\bar{R}$ is the sample's reflectance;

$$P_{atm} = \int \int_0^{\infty} I_{bb}(T_a, \lambda)\epsilon_s(\lambda, \mathit{\Omega})\epsilon_a(\lambda, \mathit{\Omega})d\lambda d\mathit{\Omega}$$

where $I_{bb}(T_a, \lambda)$ is spectral intensity of a standard blackbody with a temperature of T_a, $\epsilon_s(\lambda, \Omega)$ and $\epsilon_a(\lambda, \Omega)$ is the samples' and atmosphere's spectral emittance respectively, Ω is the solid angle;

$$P_{rad} = \ \bar{\epsilon} \times \sigma T_s^4$$

where $\bar{\epsilon}$ is the sample's emittance, σ is the Stefan–Boltzmann constant (5.67×10^{-8} J S^{-1} m^{-2} K^{-4});

$$P_c = \ h_c(T_s - T_a)$$

where h_c is the combined transfer coefficient including the heat convection and conduction.

For two samples reaching thermal equilibrium at the same condition:

$$P_{solar1} + P_{atm}(T_{a1}) = P_{rad}(T_{s1}) + P_{c1}$$

$$P_{solar2} + P_{atm}(T_{a2}) = P_{rad}(T_{s2}) + P_{c2}$$

Assuming similar emittance in two samples, the absorbed atmospheric radiation by two samples could be approximately equal. Substituting Equation S2~S5 to Equation S6~7 and subtracting Equation S6 and S7, we can get:

$$P_{ir}(\overline{R_2} - \overline{R_1}) = \bar{\epsilon}\sigma({T_{s1}}^4 - {T_{s2}}^4) + h_c(T_{s1} - T_{s2})$$

Therefore, we can evaluate the temperature difference between two samples at the same condition with given values of the solar intensity, samples' reflectance difference, emittance, non-radiative heat transfer coefficient and one sample's temperature, as exemplified by **Fig. S1**.

Supplementary Note 2: Characterizing the Diffuseness of Reflection and Glare of the Coatings

Glare, or specular reflection at high angles, is a major problem faced by white or silvery radiative cooling designs. While our colored coatings, by virtue of absorption at visible wavelengths, have reduced reflection and thus glare, we further demonstrate here that reflections off them are highly diffuse, reducing glare even further.

We first demonstrate the diffuseness by photography (**Fig. S6A**), where we compare our coatings against aluminum foil. Aluminum foil, which has a partially specular reflection, shows glare at the expected angle of reflection for a specular surface (**Fig. S6B**); in contrast, the colored coatings show little glare, and the appearance is close to that off the reflection angle (**Fig. S6C**), indicating their highly diffuse reflectivity. In addition, the bilayer and monolayer show nearly the same appearance, suggesting the specularity is not influenced by the underlayer and it's mainly due to the top-layer. Additional results are shown in **Fig. S6D** by changing the angles of light incidence and photographing the samples of all four colors at the reflection direction, indicating our colored coatings show a low specularity and highly diffuse reflection at wide angle ranges, and therefore do not cause glare.

We also measured the fraction of light that is specularly reflected from the coatings at ~0˚ and 45˚ angle of incidence using an integrating sphere. When the sample is placed at 45˚ tilt (**Fig. S7**), specular reflection will hit the top port of the integrating sphere. With the port closed (**Fig. S7A**), both diffuse (I_{diff}) and specular (I_{spec}) reflection can be recorded. When the port is removed (**Fig. S7B**), I_{spec}, the near-specular part of I_{diff} from the sample, and a small fraction of diffused light within the integrating sphere would escape through the open port, resulting in a decreased reflectance measured by the detector. For diffuse reflectors with little glare, light is reflected in all directions so the loss through the top port would be relatively small. However, for specularly reflective samples showing strong glare (I_{spec}) along the angle of reflection, much of the light would escape through the port, and the measured reflectance would be drastically lower.

As illustrated in **Fig. S7C to F** for four different colors, the reflectance reduces when the port is opened. **However, the relative reduction in R_{VIS} (22%, 21%, 19% and 33% for blue, red, yellow and black, respectively) (Fig. S7G) is close to the 20% reduction observed of a diffuse reflectance standard (Item SM05CP2C, Thorlabs) (Fig. S7H).** This means the diffuseness is similar to that of the diffuse standard. The 33% change observed for black is primarily due to its very low R_{VIS} (0.06), which amplifies the small change (0.02) when the port is opened – in the NSWIR wavelengths where the reflectance is higher, the relative reduction is ~20% (**Fig. S7H**), like the diffuse reflectance standard. The results indicate that the reflectances of the bilayer coatings are highly diffuse.

For the specularity characterization at normal incidence (0˚), since the specular reflection follows the same path as the incoming light at 0˚ (**Fig. S8A**), measuring the total reflection is not possible at normal incidence, so it was measured at 15˚ (**Fig. S8B**) instead, as reflectances of surfaces don't change significantly at low angles (*11*, *43*). The difference between the 15˚ and 0˚ measurements should indicate the extent of specularity. **Fig. S8** (**C** to **F**) shows that the difference is small, indicating that the specular component at normal incidence is small as well.

Lastly, since glare off surfaces increases more at large angles for smooth specular reflectors than rough diffuse reflectors (which are less sensitive to angle), we took reflectance measurements at 30˚ and 65˚ angles (**Fig. S9**) to see if there are any large increases in visible reflectance. However, the visible reflectance increased only by a few percent, indicating that the surface is diffuse, and that glare does not significantly increase at higher angles.

Supplementary Note 3: The Infrared Optical Properties of Commercial Paint Coatings and Bilayer Components

We have measured the infrared spectrum of the bilayer components (**Fig. S11**) and all emittance values are summarized in **Table S2**. The colored top-layers show lower emittance (0.59~0.85) (**Fig. S11D**) compared to the highly emissive underlayers (0.96) (**Fig. S11A**), which is expected because they are thin (16~55 µm) and part of infrared light passes through them without being absorbed **(Fig. S11B**). However, the transmitted infrared light is absorbed by the highly emissive underlayer (**Fig. S11A**), and since the reflectance of the top-layer is low (**Fig. S11C**) and comparable to the underlayer's reflectance (**Fig. S11A**), the top-layer doesn't significantly affect the emittance of the coatings. Consequently, the emittances of the underlayer and bilayer are both high, and typical of paint coatings (**Table S2**).

Supplementary Note 4: Solar Tests without Convection Shield

Fig. S13 shows temperatures of bilayers and monolayers of different colors when left under sunlight without a polyethylene (PE) convection shield. As evident, the P(VdF-HFP)-based bilayer is the coolest, while the monolayer is the warmest for each color. The lower temperature differences between the cases bilayers and monolayers compared to **Fig. 4** is due to larger convection and in case of the black, blue and red samples, weaker solar intensities during the time of the tests. However, the temperature differences (6.4/3.4/2.6/4.5 °C for black/blue/red/yellow samples) are still high, and significant for thermoregulation of buildings.

Additionally, we note that in certain conditions, when sunlight is weak and the solar reflectance of the coatings are high (e.g. for light yellow coatings), sub-ambient cooling can be achieved by the coatings. **Fig. S14** shows an example.

Supplementary Note 5: Sensitivity of Bilayer Coatings to Fabrication Parameters

Given that the bilayer is fabricated by successively painting two different layers with different thicknesses, we investigated the sensitivity of its optical performance to the fabrication process. The results are presented in **Fig. S16**, **S17** and **S18**. As shown in **Fig. S16**, for each color, three samples fabricated with the same coating procedure show near-identical optical properties in the solar wavelengths and infrared thermal wavelengths, indicating repeatability of the process.

We also changed the composition of the precursor solution of the P(VdF-HFP) underlayer as investigated in a previous work (*11*) to see if the fabrication process for the underlayer impacts the bilayer performance. **Fig. S17** shows that the effect of changing composition of the precursor is minimal.

We also changed the thickness of the top-layer to see its impact on the optical performance. The results for blue and yellow colors are shown in **Fig. 5** and **S18**. As evident, changing the thickness of the top layer by ~3 times only reduces the NSWIR reflectance by ~10% for either color. With regard to fabrication, this is highly desirable, as it shows that the technique is quite insensitive to top-layer thickness in terms of R_{NSWIR}. We also note that for the yellow commercial top-layer (**Fig. S18**), the visible absorptance remains the same, which is attributable to the scattering by the TiO_2 that makes even a thin top-layer optically thick in the visible. For blue (**Fig. 5**), the visible absorptance increases with thickness because the top-layer, which has the dissolved blue dye and no scatterer, is not optically thick, so absorption in the visible builds up until light reaches the underlayer. It follows that by using top layers with or without scatterer, different coarse and fine control of the visible spectrum can be achieved. Collectively, all three tests indicate the robustness of the fabrication procedure at yielding high cooling performance.

Supplementary Note 6: COMSOL Simulations

COMSOL Multiphysics v5.3 was applied to simulate the sample's steady-state temperature under sunlight. Overall heat flows are illustrated in **Fig. S19**. In the heat flux part, the sum of absorbed sunlight (P_{solar}) and atmospheric irradiance (P_{atm}) was applied on the top surface of the sample. A reflectance uncertainty of 0.01 was considered in the calculation of P_{solar}. P_{atm} was obtained by the sum of 2 parts: 4~20 μm and 20~100 μm. The radiance spectrum in the first part was obtained through MODTRAN® 6 Web Application using the method outlined by Mandal et. al.(*11*) and a blackbody emittance spectrum was used in the second part due to the atmosphere opaque property after 20 μm (*44*). In the sample radiation part, the ambient temperature was set as 0, because the atmospheric irradiation had been taken into account separately in the heat flux part. In the heat convection part, the measured air temperature inside the box was used as the ambient temperature and different convection heat transfer coefficients (h_c) were input to calculate the sample temperatures under varied convection conditions.

REFERENCES AND NOTES

1. U.S. Energy Information Administration, Annual energy outlook 2019 with projections to 2050; www.eia.gov/outlooks/aeo/pdf/aeo2019.pdf.

2. G. B. Smith, C.-G. Granqvist, *Green Nanotechnology—Solutions for Sustainability and Energy in the Built Environment* (CRC Press, 2010).

3. M. Santamouris, J. Feng, Recent progress in daytime radiative cooling: Is it the air conditioner of the future? *Buildings* **8**, 168 (2018).

4. C. G. Granqvist, A. Hjortsberg, Surfaces for radiative cooling: Silicon monoxide films on aluminum. *Appl. Phys. Lett.* **36**, 139–141 (1980).

5. C. G. Granqvist, G. A. Niklasson, Solar energy materials for thermal applications: A primer. *Sol. Energy Mater. Sol. Cells* **180**, 213–226 (2018).

6. M. M. Hossain, M. Gu, Radiative cooling: Principles, progress, and potentials. *Adv. Sci.* **3**, 1500360 (2016).

7. B. Zhao, M. Hu, X. Ao, N. Chen, G. Pei, Radiative cooling: A review of fundamentals, materials, applications, and prospects. *Appl. Energy* **236**, 489–513 (2019).

8. C. S. Wojtysiak, Radiative cooling surface coatings. Patent WO. 2002098996 (2002).

9. B. Bhatia, A. Leroy, Y. Shen, L. Zhao, M. Gianello, D. Li, T. Gu, J. Hu, M. Soljačić, E. N. Wang, Passive directional sub-ambient daytime radiative cooling. *Nat. Commun.* **9**, 5001 (2018).

10. Cool Roof Rating Council, Rated products directory; https://coolroofs.org/directory.

11. J. Mandal, Y. Fu, A. C. Overvig, M. Jia, K. Sun, N. N. Shi, H. Zhou, X. Xiao, N. Yu, Y. Yang, Hierarchically porous polymer coatings for highly efficient passive daytime radiative cooling. *Science* **362**, 315–318 (2018).

12. A. R. Gentle, G. B. Smith, A subambient open roof surface under the mid-summer sun. *Adv. Sci.* **2**, 1500119 (2015).

13. J.-L. Kou, Z. Jurado, Z. Chen, S. H. Fan, A. J. Minnich, Daytime radiative cooling using near-black infrared emitters. *ACS Photonics* **4**, 626–630 (2017).

14. N. Yu, J. Mandal, A. Overvig, N. N. Shi, Systems and methods for radiative cooling and heating. Patent WO. 2016205717 (2016).

15. A. R. Gentle, G. B. Smith, Radiative heat pumping from the earth using surface phonon resonant nanoparticles. *Nano Lett.* **10**, 373–379 (2010).

16. Y. Zhai, Y. Ma, S. N. David, D. Zhao, R. Lou, G. Tan, R. Yang, X. Yin, Scalable-manufactured randomized glass-polymer hybrid metamaterial for daytime radiative cooling. *Science* **355**, 1062–1066 (2017).

17. D. Zhao, A. Aili, Y. Zhai, J. Lu, D. Kidd, G. Tan, X. Yin, R. Yang, Subambient cooling of water: Toward real-world applications of daytime radiative cooling. *Joule* **3**, 111–123 (2018).

18. A. R. Gentle, G. B. Smith, Optimized infra-red spectral response of surfaces for sub-ambient sky cooling as a function of humidity and operating temperature. *Photon. Sol. Energy Syst. III* **7725**, 77250Z (2010).

19. E. Rephaeli, A. Raman, S. H. Fan, Ultrabroadband photonic structures to achieve high-performance daytime radiative cooling. *Nano Lett.* **13**, 1457–1461 (2013).

20. A. P. Raman, M. A. Anoma, L. Zhu, E. Rephaeli, S. Fan, Passive radiative cooling below ambient air temperature under direct sunlight. *Nature* **515**, 540 (2014).

21. Z. Chen, L. X. Zhu, A. Raman, S. Fan, Radiative cooling to deep sub-freezing temperatures through a 24-h day-night cycle. *Nat. Commun.* **7**, 13729 (2016).

22. C. Zou, G. Ren, M. M. Hossain, S. Nirantar, W. Withayachumnankul, T. Ahmed, M. Bhaskaran, S. Sriram, M. Gu, C. Fumeaux, Metal-loaded dielectric resonator metasurfaces for radiative cooling. *Adv. Opt. Mater.* **5**, 1700460 (2017).

23. S. H. Choi, S.-W. Kim, Z. Ku, M. A. Visbal-Onufrak, S.-R. Kim, K.-H. Choi, H. Ko, W. Choi, A. M. Urbas, T.-W. Goo, Y. L. Kim, Anderson light localization in biological nanostructures of native silk. *Nat. Commun.* **9**, 452 (2018).

24. N. N. Shi, C.-C. Tsai, M. J. Carter, J. Mandal, A. C. Overvig, M. Y. Sfeir, M. Lu, C. L. Craig, G. D. Bernard, Y. Yang, N. F. Yu, Nanostructured fibers as a versatile photonic platform: Radiative cooling and waveguiding through transverse anderson localization. *Light Sci. Appl.* **7**, 37 (2018).

25. T. Li, Y. Zhai, S. He, W. Gan, Z. Wei, M. Heidarinejad, D. Dalgo, R. Mi, X. Zhao, J. Song, J. Dai, C. Chen, A. Aili, A. Vellore, A. Martini, R. Yang, J. Srebric, X. Yin, L. Hu, A radiative cooling structural material. *Science* **364**, 760–763 (2019).

26. L. Cai, Y. Peng, J. Xu, C. Zhou, C. Zhou, P. Wu, D. Lin, S. Fan, Y. Cui, Temperature regulation in colored infrared-transparent polyethylene textiles. *Joule* **3**, 1478–1486 (2019).

27. L. M. Lozano, S. Hong, Y. Huang, H. Zandavi, Y. A. El Aoud, Y. Tsurimaki, J. Zhou, Y. Xu, R. M. Osgood, G. Chen, S. V. Boriskina, Optical engineering of polymer materials and composites for simultaneous color and thermal management. *Opt. Mater. Express* **9**, 1990–2005 (2019).

28. A. Synnefa, M. Santamouris, K. Apostolakis, On the development, optical properties and thermal performance of cool colored coatings for the urban environment. *Sol. Energy* **81**, 488–497 (2007).

29. G. J. Lee, Y. J. Kim, H. M. Kim, Y. J. Yoo, Y. M. Song, Colored Passive Radiative Cooler: Colored, daytime radiative coolers with thin-film resonators for aesthetic purposes (Advanced Optical Materials 22/2018). *Adv. Opt. Mater.* **6**, 1870085 (2018).

30. W. Li, Y. Shi, Z. Chen, S. Fan, Photonic thermal management of coloured objects. *Nat. Commun.* **9**, 4240 (2018).

31. H. Gonome, M. Nakamura, J. Okajima, S. Maruyama, Artificial chameleon skin that controls spectral radiation: Development of chameleon cool coating (C^3). *Sci. Rep.* **8**, 1196 (2018).

32. G. B. Smith, A. Gentle, P. Swift, A. Earp, N. Mronga, Coloured paints based on coated flakes of metal as the pigment, for enhanced solar reflectance and cooler interiors: Description and theory. *Sol. Energy Mater. Sol. Cells* **79**, 163–177 (2003).

33. G. B. Smith, A. Gentle, P. D. Swift, A. Earp, N. Mronga, Coloured paints based on iron oxide and silicon oxide coated flakes of aluminium as the pigment, for energy efficient paint: Optical and thermal experiments. *Sol. Energy Mater. Sol. Cells* **79**, 179–197 (2003).

34. J. Song, J. Qin, J. Qu, Z. Song, W. Zhang, X. Xue, Y. Shi, T. Zhang, W. Ji, R. Zhang, H. Zhang, Z. Zhang, X. Wu, The effects of particle size distribution on the optical properties of titanium dioxide rutile pigments and their applications in cool non-white coatings. *Sol. Energy Mater. Sol. Cells* **130**, 42–50 (2014).

35. X. Lu, P. Xu, H. Wang, T. Yang, J. Hou, Cooling potential and applications prospects of passive radiative cooling in buildings: The current state-of-the-art. *Renew. Sustain. Energy Rev.* **65**, 1079–1097 (2016).

36. M. Zeyghami, D. Y. Goswami, E. Stefanakos, A review of clear sky radiative cooling developments and applications in renewable power systems and passive building cooling. *Sol. Energy Mater. Sol. Cells* **178**, 115–128 (2018).

37. Mikron Instrument Company Inc., Table of emissivity of various surfaces; www-eng.lbl.gov/~dw/projects/DW4229_LHC_detector_analysis/calculations/emissivity2.pdf.

38. R. Levinson, P. Berdahl, H. Akbari, Solar spectral optical properties of pigments—Part I: Model for deriving scattering and absorption coefficients from transmittance and reflectance measurements. *Sol. Energy Mater. Sol. Cells* **89**, 319–349 (2005).

39. R. Levinson, P. Berdahl, H. Akbari, Solar spectral optical properties of pigments—Part II: Survey of common colorants. *Sol. Energy Mater. Sol. Cells* **89**, 351–389 (2005).

40. J. Schanda, *Colorimetry: Understanding the CIE System* (John Wiley & Sons, 2007).

41. Arkema, Kynar & Kynar flex PVDF performance characteristics and data (2017); https://www.extremematerials-arkema.com/en/product-families/kynar-pvdf-family/download-performance-characteristics-data-brochure/.

42. Arkema, New fluoropolymer latex technology for cool materials solutions across an expanded color space (2008); http://coolcolors.lbl.gov/assets/docs/PAC-2008-03-06/Arkema-slides.pdf.

43. J. Mandal, D. Wang, A. C. Overvig, N. N. Shi, D. Paley, A. Zangiabadi, Q. Cheng, K. Barmak, N. F. Yu, Y. Yang, Scalable, "dip-and-dry" fabrication of a wide-angle plasmonic

selective absorber for high-efficiency solar-thermal energy conversion. *Adv. Mater.* **29**, 1702156 (2017).

44. H. Karttunen, P. Kröger, H. Oja, M. Poutanen, K. J. Donner, *Fundamental Astronomy*. (Springer, 2016).